Slope three-layer scattering model for forest height estimation over mountain forest areas from L-band single-baseline PolInSAR data

Nghia Pham Minh

SPIE.

Slope three-layer scattering model for forest height estimation over mountain forest areas from L-band single-baseline PolInSAR data

Nghia Pham Minh[a,b,*]

[a]Le Qui Don Technical University, Faculty of Radio-Electronics, Hanoi, Vietnam
[b]Duy Tan University, Da Nang, Vietnam

Abstract. A slope three-layer scattering model (STSM) for retrieving forest height in mountain forest region using L-band polarimetric synthetic aperture radar interferometry (PolInSAR) data is proposed in this paper. The proposed model separates the vertical structure of forest into three layers: canopy, tree trunk, and ground layer, which account for the effect of topography for forest height calculation in a sloping forest area. Compared to the conventional two-layer random volume over ground model, the STSM improves substantial for modeling of actual mountain forest, allowing better understanding of microwave scattering process in sloping forest area. The STSM not only enables the accuracy improvement of the forest height estimation in sloping forest area but also provides the potential to isolate more accurately the direct scattering, double-bounce ground trunk interaction, and volume contribution, which usually cannot be achieved in the previous forest height estimation methods. The STSM performance is evaluated with simulated data from PolSARProSim software and ALOS/PALSAR L-band spaceborne PolInSAR data over the Kalimantan areas, Indonesia. The experimental results indicate that forest height could be effectively extracted by the proposed STSM. © *2018 Society of Photo-Optical Instrumentation Engineers (SPIE)* [DOI: 10.1117/1.JRS.12.025008]

1 Introduction

Forest is a tree-dominated plant formation that covers ∼30% of the total land area,[1] with a mean tree height of about 20 m. Forest height is important information for many management activities and is a critical parameter in modeling of ecosystem procedures. Polarimetric synthetic aperture radar interferometry (PolInSAR) system has shown great potential for forest height retrieval as it is sensitive to the vertical structure and physical characteristics of the scattering media. Fifteen years ago, several techniques had been proposed for forest height estimation using single-baseline PolInSAR image and most of them can be broken up into two categories. The first group is based on the random volume over ground model (RVoG) as presented by Cloude and Papathanassiou,[2] Yamaguchi,[3–5] and Garestier.[6–8] Among them, the three-stage inversion algorithm proposed by Cloude and Papathanassiou is quite simple and most widely used. However, in the three-stage inversion algorithm, the estimation of volume decorrelation is not very accurate, and there is an ambiguity zone of volume decorrelation. In addition, methods proposed by Yamaguchi can detect local scattering centers corresponding to the canopy top and ground in the forest area but detection accuracy of the technique becomes worse for dense forest regions due to strong volume scattering component. The second major group is based on model-based decomposition technique for PolInSAR data as reported by Ballester-Bermand[9] and Neumann

et al.[10] These methods opened a new way for the forest height estimation using target decomposition technique. However, there exits an underdetermined problem in these methods. One parameter in the surface or double-bounce scattering model is set to zero, thus leading to the instability of the decomposition. The instability of these methods will cause false forest height estimation.

On the other hand, the methods mentioned above for forest height estimation have been mostly carried out over relatively flat areas and little research has been done on slope terrain. In Ref. 2, Cloude and Papathanassiou proposed two-layer RVoG model for vegetated regions. In this model, authors assumed that the canopy extends from crown to ground and forest is placed above a little rugged surface. However, for sloping forest areas, scattered signals are strongly affected by the variation of the local incidence angle and local orientation angle (OA) due to the local topographic slope, and natural forest has significant species and age-related variations in vertical structure. Therefore, this model is difficult to obtain the high accuracy for the forest height estimation in sloping forest areas and is not able to distinguish between single- and double-bounce scattering contribution.

For these reasons, we proposed a slope three-layer scattering model (STSM) for forest height estimation over sloping forest area using L-band single-baseline PolInSAR data. The proposed model assumes that the vertical structure of forest placing on slope terrain can be separated into three layers: canopy, tree trunk, and ground layer. The boundary between the tree trunk and canopy layer is not explicitly defined but, for most trees, can be set at the first branching point, where the tree trunk divides into multiple large branches. A combining hybrid decomposition and constrained optimization iterative techniques together with generalized volume model are developed for forest parameters retrieval over sloping forest area. In the STSM, we first develop a general volume scattering model, which can be characterized by three parameters: a degree of randomness, a mean OA, and the particle scattering anisotropy. After which, we suggest that the reference volume scattering coherence matrix is used to determine the best fit parameters, which can express general volume scattering coherence matrix. The forest height inversion process is executed by the following three steps. First, an eigen-based and adaptive model-based decomposition is combined in a so-called hybrid decomposition for canopy layer parameters estimation. Second, the parameters of ground and tree trunk layers, ground and canopy phases are estimated using constrained optimization iterative techniques. Finally, the forest parameters are extracted by phase differencing between the canopy phase and underlying ground topography phase. The STSM provides the possibility to separate ground, tree trunk, and canopy layer based on the polarimetric signatures and interferometric coherence diversity. In addition, the proposed model not only enables the retrieval of the forest parameters above the tilted ground plane but also of the magnitude associated with each mechanisms. Another advantage of the proposed method is that it allows a more robust implementation and an unambiguous estimation of the ground topography as well as canopy phase. The experimental results show that accuracy of the forest height can be enhanced significantly by the STSM.

The paper is structured as follows. The STSM is expressed in Sec. 2. Forest height extraction based on the STSM is introduced in Sec. 3. The experimental results and discussion are described in Sec. 4. Finally, the conclusion is given in Sec. 5.

2 Slope Three-Layer Scattering Model in Mountain Forest Areas

2.1 Complex Polarimetric Interferometric Coherence

A monostatic, fully polarimetric SAR interferometry system is measured for each resolution cell in the scene from two slightly different look angles, two scattering matrices $[S_1]$ and $[S_2]$. In the case of backscattering in a reciprocal medium, the individual polarimetric data sets may be expressed by means of the Pauli target vector[11]

$$\vec{k}_{Pi} = \frac{1}{\sqrt{2}} [\, S_{hh}^i + S_{vv}^i \quad S_{hh}^i - S_{vv}^i \quad 2S_{hv}^i \,]^T, \tag{1}$$

where superscript T represents the vector transposition, $S_{pq}(p, q = \{h, v\})$ are the complex scattering coefficients, and $i = 1,2$ denotes measurements at two ends of the baseline.

The basic radar observable in PolInSAR is a six-dimensional complex matrix of a pixel in each resolution element in the scene, defined as

$$[T] = \langle \vec{k}\vec{k}^{*T} \rangle = \begin{bmatrix} T_1 & \Omega \\ \Omega^{*T} & T_2 \end{bmatrix} \quad \text{with} \quad \vec{k} = \begin{bmatrix} \vec{k}_1 \\ \vec{k}_2 \end{bmatrix}, \tag{2}$$

where $\langle \bullet \rangle$ denotes the ensemble average in the data processing and $*$ represents the complex conjugation. T_1 and T_2 are the conventional Hermitian polarimetric coherence matrices, which describe the polarimetric properties for each individual image separately, and Ω is a non-Hermitian complex matrix that contains polarimetric and interferometric information.

In general, the complex polarimetric interferometric coherence as a function of the polarization of the two images is given as

$$\tilde{\gamma}(\vec{\omega}) = \frac{\vec{\omega}_1^{*T}\Omega\vec{\omega}_2}{\sqrt{(\vec{\omega}_1^{*T}T_1\vec{\omega}_1)(\vec{\omega}_2^{*T}T_2\vec{\omega}_2)}} = \frac{\vec{\omega}^{*T}\Omega\vec{\omega}}{\vec{\omega}^{*T}T\vec{\omega}}, \tag{3}$$

where $\vec{\omega}_1 = \vec{\omega}_2 = \vec{\omega}$ is a three-component unitary complex vector defining the selection of each polarization stage, and $T = (T_1 + T_2)/2$.

2.2 Slope Three-Layer Scattering Model

For a tilted plane, the horizontal vector is no longer parallel to the surface, so, most polarization channels (HH, HV, VH, and VV) are affected by the tilted slope. The amount of slope-induced shift in the local OA can be visualized as the rotation of the vertical–horizontal basis vector about the line-of-sight so that the horizontal vector is again parallel to the surface. The local OA is geometrically related to topographic slopes and radar look angle, and it is a function of the azimuth slope, the range slope, and incidence angle of the flat terrain.[12] A schematic diagram depicting the radar image geometry is shown in Fig. 1.

For mountain terrain, the variation of the local incidence angle θ and the local OA ψ due to the local topography will lead to changes in the scattered signal,[12] which can be expressed as follows:

$$\tan \psi = \frac{\tan \omega}{-\tan \gamma \cos \theta_0 + \sin \theta_0}, \tag{4}$$

$$\cos \theta = -\hat{k}_i \hat{n}_g = \frac{\tan \gamma \sin \theta_0 + \cos \theta_0}{\sqrt{1 + \tan^2 \gamma + \tan^2 \omega}}, \tag{5}$$

where γ and ω are the local ground range and azimuth slopes, respectively, $\hat{k}_i$ is the incident wave vector, and $\hat{n}_g$ denotes the normal vector of sloping surface. The angle θ_0 is the incidence angle of the flat terrain. The polarimetry interferometric coherence matrix $\Omega(\psi)$ and coherence matrix $T(\psi)$ in sloping terrain can be obtained by rotation of a polarization OA, as reported in Ref. 13.

In the forest scattering at L-band, the backscattered waves can be considered as the surface scattering of ground (s), the double-bounce scattering between the ground and the tree trunks and
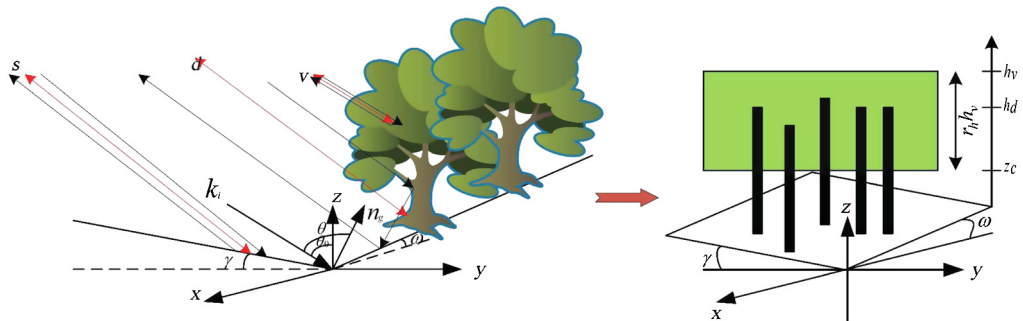

Fig. 1 STSM for mountain forest areas.

branches (d), and the volume scattering from canopy (v). In Fig. 1, the black paths and the red paths represent the true wave paths and the effective wave paths for the different component types. Considering the characteristics of forest scattering in sloping forest region and assuming that for the surface and volume components the apparent heights correspond to the true scattered heights, whereas for the double-bounce component the apparent height is located at the ground level, due to the specular reflection at the ground, the polarimetric coherence matrices and polarimetric interferometric matrix in sloping forest region then become

$$T(\psi) = m_{0v}f_v T_v + e^{-\frac{2\sigma h_v \cos\varphi}{\cos\theta}}f_g T_g + e^{-\frac{2\sigma h_v \cos\varphi}{\cos\theta}}f_d T_d,$$

$$\Omega(\psi) = e^{j\phi_v}m_{0v}f_v T_v\tilde{\gamma}_v + e^{j\phi_0}e^{-\frac{2\sigma h_v \cos\varphi}{\cos\theta}}f_g T_g\tilde{\gamma}_g + e^{j\phi_d}e^{-\frac{2\sigma h_v \cos\varphi}{\cos\theta}}f_d T_d\tilde{\gamma}_d, \qquad (6)$$

where $\phi_i\{i = g, d, v\}$ are the phase center of ground, tree trunk, and canopy layer, respectively. f_i, T_i $\{i = g, d, v\}$ represent the scattering power coefficient and coherence matrix of single-bounce, double-bounce, and volume scattering, respectively. $\tilde{\gamma}_i\{i = g, d, v\}$ denote the coherence contribution for ground, double-bounce, and volume component.

Comparing Eq. (6) with RVoG model in Ref. 2, f_d, T_d, and ϕ_d are the new parameters, which relate to double scattering interaction between the ground and tree trunks or branches, and $\cos(\varphi)$ is the new parameter account for change in the path length through canopy by local slope variation. This parameter is given as

$$\cos\varphi = \frac{1}{\sqrt{1 + \tan^2\gamma + \tan^2\omega}}, \qquad (7)$$

$$m_{0v} = \frac{\cos\theta}{2\sigma}\left(1 - e^{-\frac{2\sigma r_h h_v \cos\varphi}{\cos\theta}}\right), \quad \tilde{\gamma}_i = \int \rho_i(z')e^{jk_z'z'}\mathrm{d}z' \qquad i = \{g, d, v\}, \qquad (8)$$

where $k_z' = k_z \sin\theta_0/\sin(\theta_0 - \varphi)$, σ are the vertical wavenumber and the mean wave extinction in mountain forest areas, respectively. $\rho_i(z')$, $\{i = g, d, v\}$ represent the effective normalized backscattering strength of the given scattering-type component. Here, effective implies two aspects. One includes the attenuation effects, so that for the same density of scatters, in the presence of extinction, the backscattering strength from the lower layer will be weaker than from the upper layer. The other implies that z has to be regarded not as the true height coordinate of the scatter, but the apparent height. As shown in Fig. 1, the forest is modeled by three layers, which consist of canopy, tree trunk, and ground layers. The canopy layer is characterized by particle scattering anisotropy, the degree of orientation randomness, total forest height h_v, and the canopy-fill-factor ratio $r_h \in [0,1]$. Therefore, if mean forest height $\overline{h}_v$ is known, the coefficient r_h will be determined as follows:

$$r_h = \frac{2.7 \ln(\overline{h}_v) - 0.1}{h_v}, \qquad (9)$$

where $\overline{h}_v$ denotes the average forest height. By combining Eqs. (3), (6), and (8), the complex interferometric coherence can be obtained as

$$\begin{aligned}
\tilde{\gamma}^{\mathrm{STSM}}(\vec{\omega}) &= \frac{\vec{\omega}^{*T}\Omega(\psi)\vec{\omega}}{\vec{\omega}^{*T}T(\psi)\vec{\omega}} \\
&= \frac{e^{j\phi_v}m_{0v}f_v\vec{\omega}^{*T}T_v\vec{\omega}\tilde{\gamma}_v + e^{j\phi_g}f_g e^{-\frac{2\sigma h_v \cos\varphi}{\cos\theta}}\vec{\omega}^{*T}T_g\vec{\omega}\tilde{\gamma}_g + e^{j\phi_d}f_d e^{-\frac{2\sigma h_v \cos\varphi}{\cos\theta}}\vec{\omega}^{*T}T_d\vec{\omega}\tilde{\gamma}_d}{m_{0v}f_v\vec{\omega}^{*T}T_v\vec{\omega} + f_g e^{-\frac{2\sigma h_v \cos\varphi}{\cos\theta}}\vec{\omega}^{*T}T_g\vec{\omega} + f_d e^{-\frac{2\sigma h_v \cos\varphi}{\cos\theta}}\vec{\omega}^{*T}T_d\vec{\omega}} \\
&= \frac{e^{j\phi_v}\tilde{\gamma}_v + e^{j\phi_g}e^{-\frac{2\sigma h_v \cos\varphi}{\cos\theta}}\frac{f_g\vec{\omega}^{*T}T_g\vec{\omega}}{m_{0v}f_v\vec{\omega}^{*T}T_v\vec{\omega}}\tilde{\gamma}_g + e^{j\phi_d}e^{-\frac{2\sigma h_v \cos\varphi}{\cos\theta}}\frac{f_d\vec{\omega}^{*T}T_d\vec{\omega}}{m_{0v}f_v\vec{\omega}^{*T}T_v\vec{\omega}}\tilde{\gamma}_d}{1 + e^{-\frac{2\sigma h_v \cos\varphi}{\cos\theta}}\frac{f_g\vec{\omega}^{*T}T_g\vec{\omega}}{m_{0v}f_v\vec{\omega}^{*T}T_v\vec{\omega}} + e^{-\frac{2\sigma h_v \cos\varphi}{\cos\theta}}\frac{f_d\vec{\omega}^{*T}T_d\vec{\omega}}{m_{0v}f_v\vec{\omega}^{*T}T_v\vec{\omega}}} \\
&= e^{j\phi_g}\frac{e^{j\phi_v}\tilde{\gamma}_{0v} + \mu_1(\vec{\omega})\tilde{\gamma}_{0\,g} + e^{j\phi_d}\mu_2(\vec{\omega})\tilde{\gamma}_{0d}}{1 + \mu_1(\vec{\omega}) + \mu_2(\vec{\omega})} = e^{j\phi_g}\frac{e^{j\phi_v}\tilde{\gamma}_{0v} + \mu_1(\vec{\omega}) + e^{j\phi_d}\mu_2(\vec{\omega})}{1 + \mu_1(\vec{\omega}) + \mu_2(\vec{\omega})},
\end{aligned}$$

$$(10)$$

where $\mu_1(\vec{\omega})$ and $\mu_2(\vec{\omega})$ denote the direct ground-to-volume ratio and double-bounce ground-to-volume ratio, respectively, which are expressed as follows:

$$\mu_1(\vec{\omega}) = \frac{2\sigma}{\cos\theta\left(e^{\frac{2\sigma r_h h_v \cos\varphi}{\cos\theta}} - 1\right)} \frac{f_g}{f_v} \frac{\vec{\omega}^{*T} T_g \vec{\omega}}{\vec{\omega}^{*T} T_v \vec{\omega}}, \tag{11}$$

$$\mu_2(\vec{\omega}) = \frac{2\sigma}{\cos\theta\left(e^{\frac{2\sigma r_h h_v \cos\varphi}{\cos\theta}} - 1\right)} \frac{f_d}{f_v} \frac{\vec{\omega}^{*T} T_d \vec{\omega}}{\vec{\omega}^{*T} T_v \vec{\omega}}. \tag{12}$$

From Eq. (10) we can obtain the coherence contributions $\tilde{\gamma}_{0i}$ for any component $i \in \{g, d, v\}$ as shown in Eq. (13). The complex coherence for the volume alone $\tilde{\gamma}_{0v}$ is the function of the extinction coefficient for random volume and its thickness $r_h h_v$. The proposed STSM can be generated by marking the assumption about dual transmitter mode only. In the dual transmitter mode, we transmit and receive separately from each end of the baseline, so the phase difference across the baseline will be the same as for ground and double-bounce scattering component, with a phase corresponding to the underlying ground position. Therefore, in dual transmitter mode, the apparent effective range of heights for ground and double-bounce scattering components is located at the ground. Hence, both structure functions for ground and double-bounce components are given by a Dirac delta function and their coherence contributions $\tilde{\gamma}_{0g}$, $\tilde{\gamma}_{od}$ all equal unity.[14] For completeness, all these coherences terms need to multiplied with $e^{j\phi_g}$, which represents the baseline-dependent ground reference phase

$$e^{-j\phi_g}\tilde{\gamma}_v = \tilde{\gamma}_{0v} = e^{jk_z' h_v \cos\varphi} \frac{p_1\left(e^{p_2 r_h h_v \cos\varphi} - 1\right)}{p_2\left(e^{p_1 r_h h_v \cos\varphi} - 1\right)} = \left\{ \begin{array}{l} p_1 = \frac{2\sigma}{\cos\theta} \\ p_2 = p_1 + jk_z' \end{array} \right.,$$

$$e^{-j\phi_g}\tilde{\gamma}_d = \tilde{\gamma}_{0d} = \int_0^{h_v \cos\varphi} \delta(z')e^{jk_z' z'}\mathrm{d}z' = 1,$$

$$\tilde{\gamma}_{0g} = \int_0^{h_v \cos\varphi} \delta(z')e^{jk_z' z'}\mathrm{d}z' = 1. \tag{13}$$

Figure 2 shows the relationship between the complex polarimetry interferometric coherence and the ratio of direct ground to volume and double-bounce ground to volume. As outlined in Fig. 2, when $\mu_1(\vec{\omega})$ and $\mu_2(\vec{\omega})$ simultaneously approach zero, the complex polarimetric interferometric coherence of proposed model is close to a constant. The limit of the interferometric coherence can be deserved from

$$\lim_{\substack{\mu_1(\vec{\omega})\to 0 \\ \mu_2(\vec{\omega})\to 0}} \tilde{\gamma}^{\mathrm{STSM}}(\vec{\omega}) = e^{j\phi_g}e^{j\phi_v}\tilde{\gamma}_{0v}. \tag{14}$$

Especially, by assuming $\mu_2(\vec{\omega}) = 0$, the complex interferometric coherence of STSM becomes exactly the same as the three-layer RVoG,[2,15] whereas when $\mu_1(\vec{\omega})$ or $\mu_2(\vec{\omega})$ is constant, in other words, they are polarization-independent parameters, the locus of the interferometric coherence represents a straight line inside the unit circle in the complex coherence plane.[16]

The inversion model for the STSM can be formulated as follows:[17]

$$\underline{p} = M^{-1}\underline{\varrho} \quad \underline{p} = \{\sigma, h_v, h_d, \phi_g, \mu_1^j, \mu_2^j\} \qquad j = 1, 2, 3, \quad \underline{\varrho} = (\tilde{\gamma}_1, \tilde{\gamma}_2, \tilde{\gamma}_3), \tag{15}$$

where the operator $[M]$ represents the scattering model as given in Eqs. (10)–(13), which relates the three optimal complex coherence $(\tilde{\gamma}_j, j = 1, 2, 3)$ obtained by polarimetric interferometric phase coherence optimization[2] to 10 unknown parameters $\{\sigma, h_v, h_d, \phi_g, \mu_1^j, \mu_2^j\}$ $j = 1, 2, 3$ of the scattering process. This is a nonlinear parameter optimization problem. However, these unknown parameters cannot be directly achieved by single-baseline PolInSAR. To improve accuracy forest parameters estimation, parameters of volume scattering coherence matrix are first extracted by hybrid decomposition technique with a generalized volume model. Then, the
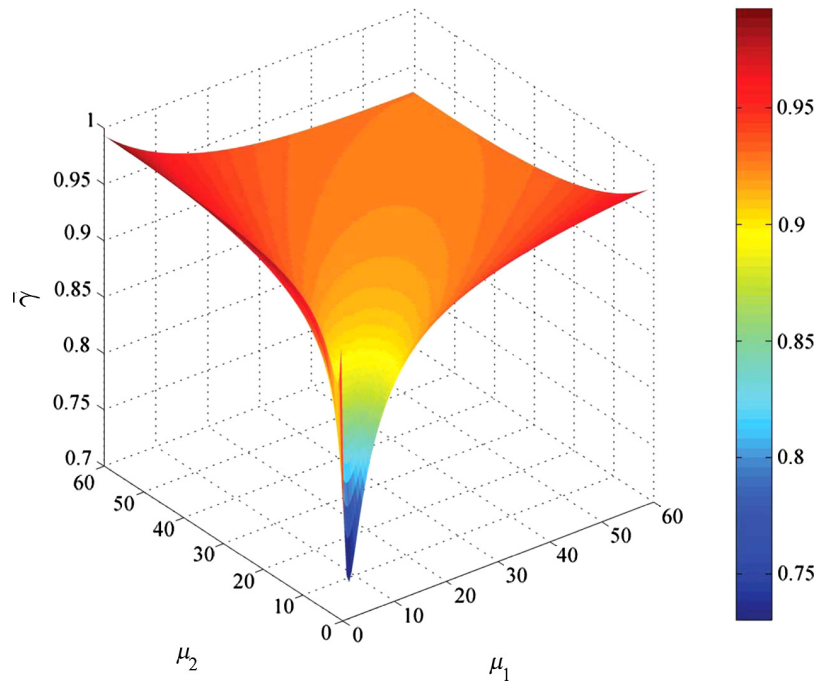
Fig. 2 Coherence amplitude variation against $\mu_1(\vec{\omega})$ and $\mu_2(\vec{\omega})$ in scattering model.

underlying ground topography, canopy phase, and parameters of surface and tree trunk are estimated using constrained optimization iterative techniques.

3 Forest Height Extraction Based on STSM

3.1 Canopy Parameters Estimation Using the Hybrid Decomposition Technique for PolInSAR

In this section, we have proposed an approach for the estimation of the canopy phase using hybrid decomposition technique for PolInSAR image. For PolInSAR data, the polarimetric coherence matrices and polarimetric interferometric coherence matrix after rotation by OA are decomposed into the three scattering mechanism corresponding to single-bounce, double-bounce, and volume scattering.[10]

$$T(\psi) = f_g[T_g(\chi)] + f_d[T_d(\chi)] + f_v[T_v(\overline{\theta})]$$
$$\Omega(\psi) = e^{j\phi_g}f_g[T_g(\chi)] + e^{j\phi_d}f_d[T_d(\chi)] + e^{j\phi_v}f_v[T_v(\overline{\theta})], \tag{16}$$

where $T_g(\chi)$, $T_d(\chi)$, and $T_v(\overline{\theta})$ represent the coherence matrix for the ground scattering, double-bounce scattering, and volume scattering component in mountain forest areas, respectively.

The volume scattering is direct diffuse scattering from the canopy layer of forest model. In mountain forest area, volume scattering component is not much affected by the tilt of the ground surface because trees on a slope grow in alignment with gravity and sunlight. In the theoretical, the scattering from the canopy layer of forest can be characterized by a cloud of randomly oriented infinitely thin cylinder, and it is implemented with a uniform probability function for OA.[18] However, for forest areas where vertical structure seems to be rather dominant, the scattering from tree trunks and branches displays a nonuniform angle distribution. Therefore, we assume that the volume scattering contribution with a von Mises distribution of orientation with probability density function as Ref. 10. This function can be characterized by two parameters: the mean orientation of particles $\overline{\theta}$ and the degree of orientation randomness τ. The mean orientation

$\overline{\theta} \in [-\pi/2; \pi/2]$ and the degree of orientation randomness τ vary from a range between 0 and 1. In order to improve the general for volume component, we add the scattering particle anisotropy in the volume coherence matrix, where $|\delta| \in [0; \sqrt{2}]$ and $\arg(\delta) = \arg\{\langle (S_{hh} + S_{vv})S_{hv}^* \rangle\}$. Therefore, T_v is a generalized volume scattering matrix, which depends on the mean OA $\overline{\theta}$, degree of randomness τ, and the particle scattering anisotropy δ. As demonstrated in the [appendix](), the volume scattering coherence matrix is given as

$$[T_v(\delta, \overline{\theta}, \tau)] = [T_a(\delta)] + p(\tau)[T_b(\delta, 2\overline{\theta})] + q(\tau)[T_c(\delta, 4\overline{\theta})]. \tag{17}$$

The coefficients $p(\tau)$ and $q(\tau)$ are characteristic by fifth-order polynomials as in Eq. (48). The basic coherence matrices $[T_a(\delta)]$, $[T_b(\delta, 2\overline{\theta})]$, and $[T_c(\delta, 4\overline{\theta})]$ are expressed as in Eq. (46).

Based on the assumptions about volume scattering mechanism, we shall develop an algorithm to estimate parameters of volume scattering component. In practically, in forest areas, the backscattering of an electromagnetic wave depends on the shape, size, and orientation of the leaves, small braches, and tree trunks; and cross-polar response is generated by volume scatters.[19] Therefore, we employed a volume scattering mechanism model in Ref. [10] as a reference volume scattering model. The model does not require any geophysical media symmetry assumption. The model is not only suitable for geophysical media symmetry but also satisfies the conditions for geophysical media asymmetry.

In this article, the reference volume scattering coherence matrix can be used to determine the best fit parameters to express the general volume scattering coherence matrix. We first determine the reference coherence matrix T_v^{ref} as in Ref. [10]. Then, we solve the volume scattering coherence matrix so that $T_v(\delta, \overline{\theta}, \tau)$ approximates to the reference volume scattering coherence matrix by varying degree of randomness τ, mean OA $\overline{\theta}$, and particle scattering anisotropy δ in their entire range. These parameter sets are equivalent to a best fit under condition that the Frobenius norm of subtraction between general volume scattering coherence matrix and reference volume scattering coherence matrix becomes minimum. Therefore, the optimization criteria is

$$\min : \|[T_{v-\text{ref}}] - [T_v(\delta, \overline{\theta}, \tau)]\|_2. \tag{18}$$

Once the parameters of the optimal volume coherence matrix are determined, subtraction of $[T_v(\delta, \overline{\theta}, \tau)]$ from $[T(\psi)]$, $[\Omega(\psi)]$ by considering the still unknown, volume coherence f_v and canopy phase ϕ_v leads to ground $[T_g(\chi)]$ and double-bounce $[T_d(\chi)]$ scattering component.

$$[T(\psi)] - f_v[T_v(\delta, \overline{\theta}, \tau)] = f_g[T_g(\chi)] + f_d[T_d(\chi)] = [T_{GD}(\chi)]$$
$$[\Omega(\chi)] - e^{j\phi_v}f_v[T_v(\delta, \overline{\theta}, \tau)] = e^{j\phi_g}f_g[T_g(\chi)] + e^{j\phi_d}f_d[T_d(\chi)] = [\Omega_{GD}(\chi)]. \tag{19}$$

The eigenvalues of two matrices $[T_{GD}(\psi)]$ and $[\Omega_{GD}(\psi)]$ are determined by eigen-decomposition techniques, confined to zero, and then we can obtain canopy phases $\phi_v^i\{i = 1, 2, 3\}$ and the volume coefficients $f_v^i\{i = 1, 2, 3\}$ as follows:

$$f_v^1 = \frac{T_{12}^* T_{v(12)} - T_{22}T_{v(11)} + T_{12}T_{v(12)}^* - T_{11}T_{v(22)} + \sqrt{AT}}{2(|T_{v(12)}|^2 - T_{11}T_{22})},$$

$$f_v^2 = \frac{T_{12}^* T_{v(12)} - T_{22}T_{v(11)} + T_{12}T_{v(12)}^* - T_{11}T_{v(22)} - \sqrt{AT}}{2(|T_{v(12)}|^2 - T_{11}T_{22})},$$

$$AT = (T_{22}T_{v(11)} - T_{12}^* T_{v(12)} - T_{12}T_{v(12)}^* + T_{11}T_{v(22)})^2$$
$$- 4(|T_{12}|^2 - T_{11}T_{22})(|T_{v(12)}|^2 - T_{v(11)}T_{v(22)}),$$

$$f_v^3 = \frac{T_{33}}{T_{v(33)}}, \tag{20}$$

$$\phi_v^1 = \arg\left(\frac{\Omega_{12}^* T_{v(12)} - \Omega_{22} T_{v(11)} + \Omega_{12} T_{v(12)}^* - \Omega_{11} T_{v(22)} + \sqrt{BT}}{2(|T_{v(12)}|^2 - \Omega_{11}\Omega_{22})}\right),$$

$$\phi_v^2 = \arg\left(\frac{\Omega_{12}^* T_{v(12)} - \Omega_{22} T_{v(11)} + \Omega_{12} T_{v(12)}^* - \Omega_{11} T_{v(22)} - \sqrt{BT}}{2(|T_{v(12)}|^2 - \Omega_{11}\Omega_{22})}\right),$$

$$BT = (\Omega_{22} T_{v(11)} - \Omega_{12}^* T_{v(12)} - \Omega_{12} T_{v(12)}^* + \Omega_{11} T_{v(22)})^2$$
$$- 4(|\Omega_{12}|^2 - \Omega_{11}\Omega_{22})(|T_{v(12)}|^2 - T_{v(11)} T_{v(22)}),$$

$$\phi_v^3 = \arg\left(\frac{\Omega_{33}}{T_{v(33)}}\right), \tag{21}$$

where Ω_{ij}, T_{ij}, and $T_{v(ij)}$ represent the element of the column j and the row i of the matrix $\Omega(\psi)$, $T(\psi)$, and T_v, respectively.

3.2 Parameters of Ground and Tree Trunk Layer Extracted From Single Baseline PolInSAR Data

In the mountain forest areas, the presence of topography variations induces a local coordinate system in accordance with the tilted ground surface. In order to address the local orientation of ground scattering term in the mountain forest areas, the flat ground scattering term of the forest scattering model are superseded by the scattering from the slanted ground plane.[20] In this case, the coherence matrix for the single- and double-bounce contribution is obtained from the rotation of an OA χ expressed as[21]

$$[T_g(\chi)] = \begin{bmatrix} 1 & \beta\eta & 0 \\ \beta^*\eta & |\beta|^2\kappa & 0 \\ 0 & 0 & |\beta|^2(1-\kappa) \end{bmatrix} \qquad [T_d(\chi)] = \begin{bmatrix} |\alpha|^2 & \alpha\eta & 0 \\ \alpha^*\eta & \kappa & 0 \\ 0 & 0 & (1-\kappa) \end{bmatrix}, \tag{22}$$

where two parameters $\eta = \int \cos 2\chi p(\chi)\mathrm{d}\chi$ and $\kappa = \int \cos^2 2\chi p(\chi)\mathrm{d}\chi$ account for the effect of slope terrain on surface and double-bounce scattering mechanisms, both of which are related to the arbitrary distribution function. The parameter κ lies between 0.5 and 1 and η varies from a range between 0 and 1.[10] Two parameters α and β are the parameter of the double-bounce and surface scatterings as proposed by Freeman-Durden.[18]

To find the best fit forest parameters, $\{f_i, \phi_i, \alpha, \beta, \kappa, \eta\}$ $(i = g, d, v)$ a constrained optimization iterative technique is implemented. With each triple value (f_v, κ, η), the parameters of ground and tree trunk layer $\{f_g, \alpha, f_d, \beta\}$ can be obtained by solving the following constrained optimization problem:

$$\text{minimize}: F = |\alpha|^2 + |\beta|^2 \quad \text{Subject to}: \begin{cases} T_{11}(\psi) = f_g + f_d|\alpha|^2 + f_v T_{v(11)} \\ T_{22}(\psi) = f_g|\beta|^2\kappa + f_d\kappa + f_v T_{v(22)} \\ T_{12}(\psi) = f_g\beta\eta + f_d\alpha\eta + f_v T_{v(12)} \\ \frac{f_g}{f_d} = M^3 \end{cases}, \tag{23}$$

where $T_{ij}(\psi)$ denotes the elements of the coherence matrix $T(\psi)$ and

$$M = \frac{G[T(\psi), \mathrm{diag}(1,0,0)]}{G[T(\psi), \mathrm{diag}(0,1,0)]},$$

represents a ratio of the similarity parameter between $T(\psi)$ and the coherence matrix of a plate to that between $T(\psi)$ and the coherence matrix of a diplane.[22,23]

In Eq. (23), the first three constraints are obtained from comparing elements of the matrix $T(\psi)$ to the coherence matrix elements of single-bounce, double-bounce, and volume scattering mechanisms. We show that the similarity parameter is an efficient feature for interpreting the polarimetric characteristic of targets, so, there exists a useful correlation between the contribution of the scattering component and the similarity parameter generated by the corresponding standard coherence matrices. Therefore, the last constraint in Eq. (23) represents the relationship

between the ratio of f_g to f_d and the similarity parameter ratio M.[24] However, the constraints alone are unable to completely determine the parameter of single- and double-bounce scattering components. So, we incorporate $F = |\alpha|^2 + |\beta|^2$ as the optimum objective function, which chooses the smallest $|\alpha|^2$ and $|\beta|^2$ as the solution when no prior information about the ground truth is available and ensure that the coefficients f_g and f_d are not negative.

In order to solve the optimization problem presented in Eq. (23), an efficient algorithm is established. The constrain in Eq. (23) can be simplified as

$$B = \frac{A + |\alpha|^2}{1 + A|\beta|^2}, \tag{24}$$

$$C = \frac{\alpha + A\beta}{A + |\alpha|^2}, \tag{25}$$

where $A = M^3$, $B = \kappa \frac{T_{11}(\psi) - f_v T_{v(11)}}{T_{22}(\psi) - f_v T_{v(22)}}$, and $C = \frac{1}{\eta} \frac{T_{22}(\psi) - f_v T_{v(12)}}{T_{11}(\psi) - f_v T_{v(11)}}$.

The constrain in Eq. (24) represents a line in the $(|\alpha|^2, |\beta|^2)$ coordinate plane for each of triple value (f_v, κ, η). The line starts from $(|\alpha|_0, |\beta|_0) = (0, \sqrt{(A-B)/AB})$ if $A \geq B$, and $(|\alpha|_0, |\beta|_0) = (\sqrt{B-A}, 0)$ if $A \leq B$. On the line, the value of the object function $F = |\alpha|^2 + |\beta|^2$ increases with increasing distance from start point. With each triple value (f_v, κ, η), the unknown parameters $|\alpha|$ and $|\beta|$ are determined by solving the constraints optimization problem. The solution of the optimization problem is the closet point to the start point on the line, with $|\alpha|$ and $|\beta|$ satisfying the constraint in Eq. (24).

For the constrain in Eq. (24), the relationship between A and B determines the sign of $|\alpha| - A|\beta|$. Therefore, Eq. (25) is transformed equivalent into the following equation:

$$\begin{cases} A|\beta| - |\alpha| \leq (A + |\alpha|^2)|C| \leq |\alpha| + A|\beta| & A \geq B \\ |\alpha| - A|\beta| \leq (A + |\alpha|^2)|C| \leq |\alpha| + A|\beta| & A \leq B \end{cases}. \tag{26}$$

If the start point of the line satisfies Eq. (26), the start point $(|\alpha|_0, |\beta|_0)$ is the solution of the optimization. Otherwise, the solution is on the boundary of the inequalities because $|\alpha| - A|\beta|$, $A|\beta| - |\alpha|$, $(A + |\alpha|^2)|C|$, and $|\alpha| + A|\beta|$ are all continuous with respect to $|\alpha|^2$ and $|\beta|^2$. The boundary is $||\alpha| - A|\beta|| = (A + |\alpha|^2)|C|$ if $||\alpha|_0 - A|\beta|_0| > (A + |\alpha|_0^2)|C|$ and $|\alpha| + A|\beta| = (A + |\alpha|^2)|C|$ if $(A + |\alpha|_0^2)|C| > |\alpha|_0 + A|\beta|_0$. The optimization algorithm needs to solve a system of two variables $|\alpha|$ and $|\beta|$, which can be transformed into a quartic equation with one unknown $|\alpha|$ or $|\beta|$. Therefore, the optimization algorithm can be solved directly using Vieta's formulae. Since the parameter set $\{f_i, \phi_i, \alpha, \beta, \kappa, \eta\}$ $(i = g, d, v)$ in this step is determined from condition minimum of Frobenius norm of matrix $T^{\text{sub}} = T(\psi) - \sum_{i=g,v,d} f_i T_i$. We show that the parameter set $\{f_i, \phi_i, \alpha, \beta, \kappa, \eta\}$ $(i = g, d, v)$ is equivalent to the best fit under the condition that the Frobenius norm of matrix T^{sub} becomes zero, where the estimated parameters are perfectly matched to the observations. Finally, we repeat above steps for each pixel in the image. When the optimal forest parameters are retrieved from STSM, we can extract surface topography phase as

$$\phi_g = \arg\left\{\frac{\kappa\Omega_{11}(\psi) - |\alpha|^2\Omega_{22}(\psi) - VT}{1 - \kappa|\alpha|^2|\beta|^2}\right\}, \quad VT = f_v e^{j\phi_v}(\kappa T_{v(11)} - |\alpha|^2 T_{v(22)}). \tag{27}$$

Based on the obtained optimization parameters from the STSM, the forest height in mountain forest areas can be extracted using the phase differencing as follows:

$$h_v = \frac{\phi_v - \phi_g}{k_z'} = \Delta\phi \frac{\lambda}{4\pi} \frac{R \sin(\theta - \varphi)}{B_n}, \tag{28}$$

where θ is the local angle of incidence over mountain forest areas, R is the distance between radar and an observed point, B_n is the normal component of the baseline, and λ is the wavelength.

4 Experimental Results and Discussion

In this section, the effective evaluation of the proposed approach is addressed but primarily in terms of the retrieved forest height estimation and ground phase. For such a purpose, we have applied the proposed method to a data set acquired from PolSARProSim software by William,[25] as well as spaceborne data acquired by the ALOS-PALSAR system.

4.1 *Simulated PolInSAR Data*

The proposed approach has first been evaluated with the simulated forest scenario and considering different slope terrains, which is generated with the PolSARProSim software. Figure 3(a) shows a red, green, and blue (RGB) coding Pauli image of the forest scenario considered with slope terrain under the system parameters shown in Table 1. Figure 3(b) is a plot of the forest height estimation of the proposed approach compared with the three-stage inversion process in the 134th row of azimuth transect line.

Compared with the three-stage inversion and adaptive model-based decomposition method with OA compensation, the proposed method provides improved results. The OA compensation decreases HV-polarization backscatters and increases the HH-polarization backscatters, but the accuracy of the adaptive model-based decomposition method becomes inappropriate by the closer two phase centers. The three-stage inversion is the most used coherence model for coherence optimization, in which ground topography can be retrieved using line fit method. While, the forest height can be estimated by taking observations of the complex coherence values at a number of difference polarization channels and then minimizing the difference between the model predictions and observation in a least square sense. Therefore, accurate forest height estimation of the three-stage inversion process depends significantly on the accurate estimation of model prediction. Moreover, when this method is used for forest height estimation in mountain forest areas, it induces the overestimation of forest height. This is caused by the variations of polarimetric interferometric coherence due to the local topographic slope. Otherwise, the forest height and extinction estimation by using three-stage inversion process is not reliable, and only the

(a)

(b)
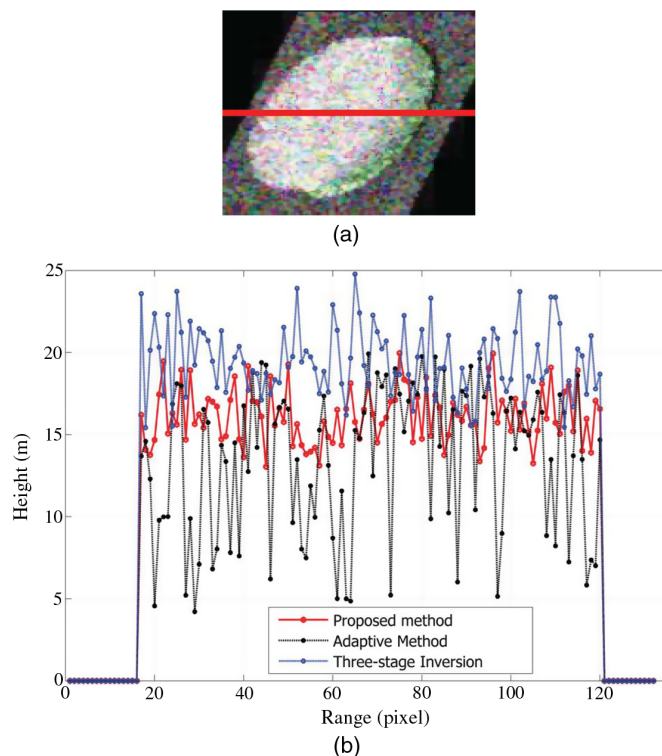
Fig. 3 (a) Pauli image on RGB coding of simulated data and (b) plot of the height results comparison.

Table 1 Values of simulation parameters.

Altitude	Look angle	Horizontal baseline	Vertical baseline	Central frequency
3000 m	30 deg	10 m	1 m	1.3 GHz
Range slope	Azimuth slope	Tree species	Tree height	Density
11.3 deg	5.7 deg	Pine	18 m	600 stem/Ha

Table 2 Forest parameters estimation for three methods.

Parameters	True value	Three stage inversion	Adaptive method	STSM
h_v (m)	18	19.3078	15.9030	17.4580
h_d (m)	10.8	—	8.2052	9.8827
r_h	0.6	—	0.4977	0.5314
Φ_0 (rad)	−0.148	−0.1516	−0.1368	−0.1406
RMSE (m)	—	3.1453	2.8286	2.8095

Table 3 Forest parameters estimation for difference slope terrain by STSM.

Parameter	True	$\gamma = 11.3$ deg $\omega = 5.7$ deg	$\gamma = 21.8$ deg $\omega = 5.7$ deg	$\gamma = 30.9$ deg $\omega = 5.7$ deg	$\gamma = 11.3$ deg $\omega = 16.7$ deg	$\gamma = 11.3$ deg $\omega = 21.8$ deg	$\gamma = 21.8$ deg $\omega = 16.7$ deg	$\gamma = 30.9$ deg $\omega = 26.6$ deg
h_v (m)	18	17.4580	17.6424	18.0777	17.7557	18.3228	18.5814	19.1290
h_d (m)	10.8	9.8827	10.1334	11.4548	10.1582	11.3154	11.8395	12.8301
r_h	0.6	0.5314	0.4397	0.4490	0.4659	0.4604	0.4927	0.5202
Φ_0 (rad)	−0.148	−0.140	−0.134	−0.111	−0.107	−0.119	−0.106	−0.092
RMSE (m)	—	2.8095	3.2376	3.2714	3.2497	3. 4135	4.3297	4.9562

underlying ground topographic phase is reliable. Based on Fig. 3 and Table 2, we can say that the forest height and ground phase estimation using STSM are more accurate and reliable than using three-stage inversion method and adaptive model-based decomposition method.

Changes in the scene parameters can be noticed by means of the proposed method. Table 3 shows the forest parameters estimation with difference slope terrains. The rest of parameters remain unchanged. The interferometric phase is affected remarkably by both azimuth and ground ranges slopes. So, the forest height estimation methods related to phase will hard to obtain the right value.[26] In the proposed method, the accuracy of forest height estimation is significantly improved by orientation compensation and choosing the best fit parameter for each scattering mechanism based on the constrained optimization. From Table 3, we show that the local ground range slopes γ from 11.3 deg (20%) to 30.9 deg (60%) and the local ground azimuth slope ω all range from 5.7 deg (10%) to 26.6 deg (50%). Table 3 shows that the forest height increases slightly when range terrain slope increases, and it increases significantly when azimuth terrain slope increases. Especially, the forest height is overestimated at $(\gamma, \omega) = (30.9 \text{ deg}, 26.6 \text{ deg})$, but the error estimation of it is relatively slight, which equals 6.3%. Based on Table 3, we can say that the proposed STSM model and inversion procedure can be able to correct the terrain

distortion effectively and provide much more accurate estimation of forest height than the RVoG model.

4.2 *Spaceborne PolInSAR Data*

Next, we have also evaluated the proposed method with spaceborne PolInSAR data. The data set used in this paper is acquired from an image pair of the Kalimantan region, Indonesia, by the ALOS/PALSAR system, observed on March 12 and April 27, 2007, respectively. The baseline of the two observations is 330 m at the scene center. The spatial resolution of the test data is 30 m × 10 m. They consist of full polarized data at L-band with 21.5 deg angle of incidence and composed of 12,816 × 1129 pixels. The optical image from Google Earth and the color image of the classical Pauli decomposition are shown in Figs. 4(a) and 4(b), respectively. The Kalimantan area that contains heterogeneous objects such as forest area, agricultural area (violet area), and mountains is covered with trees. As analyzed by Papathanassiou,[26] the presence of temporal correlation coefficient leads to a decrease of the amplitude of the interferometric coherence but do not affect the position of the effective phase centers. Furthermore, the amplitude of the interferometric coherence of test site data (after coregistration image and filtering procedures) almost greater than 0.65 and the forest height of proposed method is estimated using the difference phase method. Hence, in this section, we neglect the effect of the temporal decorrelation.

After coregistration of PolInSAR images, we select two regions of interest from Fig. 4(b) for further comparison, including mountain forest area A with 521 pixels in range and 237 pixels in azimuth, the forest B with 306 × 468. Patch B contains mainly pure forest, whereas patch A includes almost mountain which is covered with trees. The coding Pauli images of two ROI are represented in Fig. 5.

Figure 6(a) is a plot of the forest height estimation of the proposed approach compared with adaptive model-based decomposition[27] with OA compensation in patch A. This figure shows that the forest height of proposed approach is located in a range from 13 to 32 m (except at pixel 186 in the range the forest height is about 5 m), while the forest height of adaptive model-based decomposition method is located in a range from 3 to 29 m. The parameters of forest over two patches are estimated and shown in Table 4. This table indicates that forest parameters estimation of the proposed STSM is more accurate and less error prone than that of the adaptive model-based decomposition approach. Even though the adaptive model-based decomposition approach was compensated for the effect of topography variations by the rotation coherence matrix of an OA. Orientation angle compensation can reduce these cross-polarization powers, and better decomposition performance can be achieved. However, the estimated polarization OA is a mixture among all the scattering mechanisms for a coherence matrix. So, this approach cannot

(a)　　　　　　　　(b)
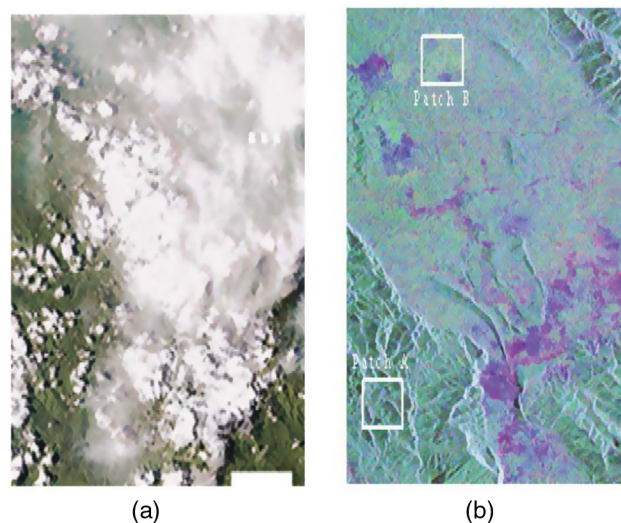
Fig. 4 L-band PALSAR data of Kalimantan region. (a) Optical image and (b) Pauli decomposition.

(a)

(b)
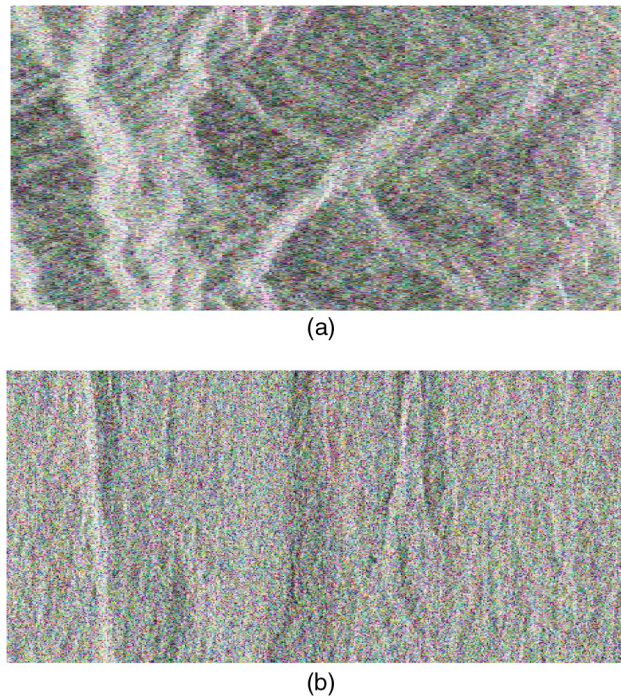
**Fig. 5** The coding Pauli image of two ROI. (a) Mountain forest area A and (b) forest area B.

always guarantee for cross-polar of the single- and double-bounce scattering contributions back to zero. This is a possible reason that the canopy phase and underlying ground phase estimation ambiguity still appears, especially at the mountain forest areas.

Figure 6(b) shows the estimated forest height by using STSM in mountain forest A. In this figure, it is shown that the most of the peak differential of the forest height is located at ∼20 m. The actual forest heights are quite well retrieve, except at some pixels are overestimated but almost of forest heights in these pixels are all less than 35 m. The real effective tree height will be higher than these values so we can say that the results are acceptable.

Based on Fig. 6 and Table 4, we can say the forest height and the underlying ground topographic phase estimation in mountain forest areas by using the STSM. Consequently, the STSM model and proposed approach provide relative accuracy with small error and more accurate for vertical structural variations especially at the sloping terrain.

In order to estimate the main forest parameters, the presented forest model in the alternate transmit mode is used. The parameter inversion process consists a constrained optimization iterative technique and estimating the physical parameters $\{\sigma, h_v, h_d, \phi_g, f_g, f_d, \alpha, \beta, \overline{\theta}, \tau, \delta\}$. Figure 7 presents the parameter inversion performance for the forest place on mountain A over the 200th row. The height sensitivity is given by the vertical wavenumber, which is about 0.16. This corresponds to 2π height ambiguity of about 40 m. In the experiments, the graphs display the value and the standard deviation of estimated parameters. The results indicate that the total forest height is around 20 m, the underlying topography phase varies in range from -0.5 to 0.5 rad, the volume power is about 0.5 of the total power, the degree of orientation randomness is low $\tau \approx 0.3$, the mean orientation of canopy ranges from -74.5 deg to 0 deg and extinction around 0.02 dB/m.

With unitary complex vector $\vec{\omega} = [\cos \xi \quad \sin \xi \quad 1]$, where $\xi = \arctan(|\alpha|^2)$, we can determine the double-bounce ground-to-volume ratio as in Eq. (12), and then the backscattering intensity ratios of the direct ground to volume is extracted from Eq. (10). The backscattering intensity ratios $\mu_1(\vec{w})$ in three different polarization channels (HH, HV, and VV) in the 200th row of patch A are shown in Fig. 8. We know that HV-polarization channel always is taken to be complex volume coherence, as this channel is dominated by volume scattering. So, the backscattering intensity ratios for HV channel are relatively low, almost less than 1. Comparing with Fig. 5(a) we show that the pixel 143 corresponds to the canyon, so this ratio at this pixel is ∼1.5.
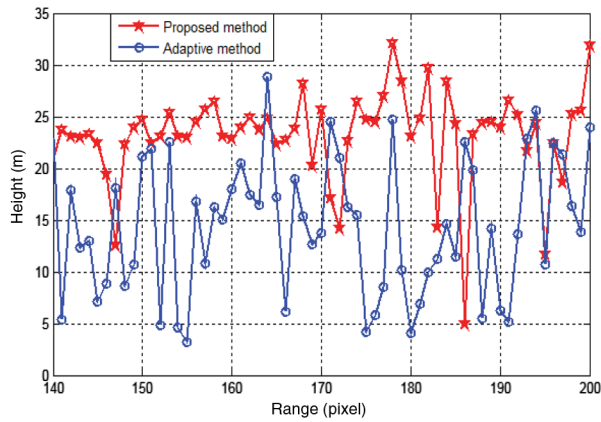
(a)
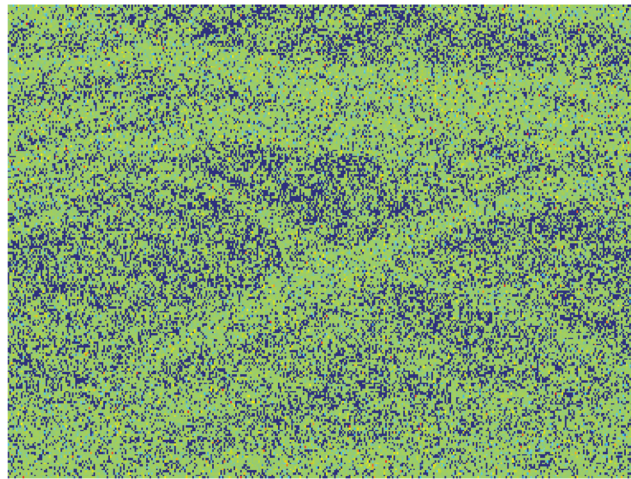
(b)

Fig. 6 Forest height estimation over forest mountain A. (a) Plot of the height results comparison. (b) Forest height estimation based on the STSM.

Otherwise, the HH and VV polarization channels relate to the topography, as these channels are dominated by single-bounce scattering. Therefore, the backscattering intensity ratios for HH and VV channels are relatively higher but almost less than 1. Except at some pixels (143 to 145, 176, 186, and 195), the single-bounce scattering component is dominant so the backscattering intensity ratios are greater than 1.5 (these pixels all correspond to canyon). Figure 8 indicates that the ground-to-volume amplitude ratio can be accurately extracted by STSM.

Table 4 Forest parameters estimation for two approaches over two study areas.

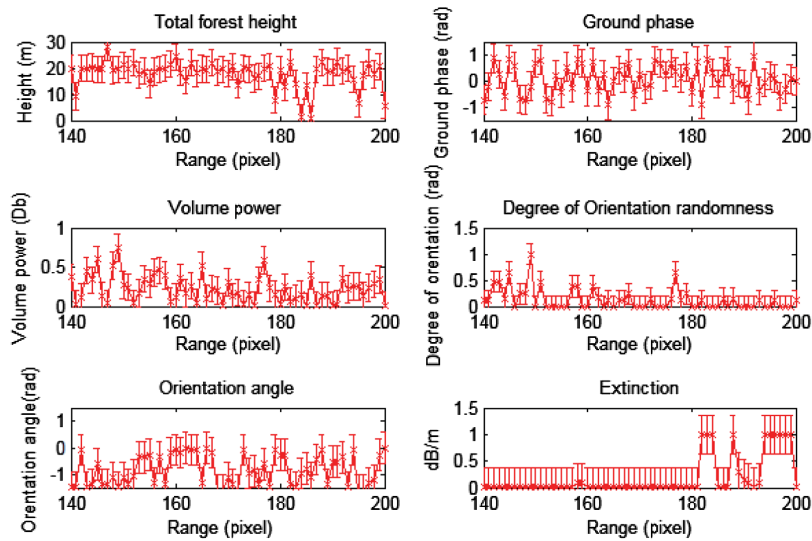|	Patch A		Patch B	
	Adaptive	STSM	Adaptive	STSM
h_v (m)	17.8210	19.5233	17.7214	19.3249
h_d (m)	12.2334	15.1064	12.2052	15.0871
r_h	0.4576	0.4244	0.4577	0.5418
Φ_1 (rad)	−0.0180	−0.0145	0.0068	−0.0182
RMSE (m)	3.6974	3.2674	3.5494	3.2158
σ (dB/m)	0.2411	0.2112	0.1825	0.2178

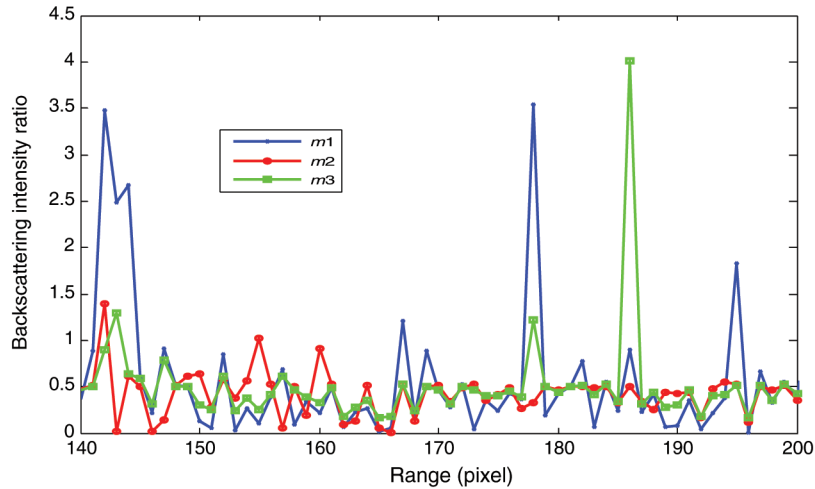**Fig. 7** Parameter estimation for mountain forest area A.

Fig. 8 The direct ground-to-volume ratio for three polarization channels in 200th row.

To evaluate the proposed model further, the derived scattering power by using the proposed approach and the adaptive model-based decomposition method with orientation compensation corresponding to the mountain forest A and forest B are shown in Table 5. For forest area B, which corresponds to a small rugged area, the two methods show relatively equivalent results. In this area, the volume scattering is dominant and very high, 88.25% for adaptive decomposition and 90.41% for the proposed method. For mountain forest area A, for the adaptive decomposition, although the volume scattering component is still dominant, the percentage of dominant P_v is reduced to 69.53% while the percentage of dominant single- and double-bounce contributions P_s and P_d are increased to 11.86% and 18.617%, respectively. For the proposed STSM, even though the dominant volume scattering is still maximal but the percentage of dominant P_v is significantly decreased to 61.85%. Otherwise, the percentage of surface scattering component P_s is significantly increased to 21.19%. The percentage of double bounce is relatively increased to 16.96%. The reason lies in that the scattering mechanisms in patch A is strongly affected by the topographic variations. In addition, the topographic variations induce changes in the penetration depth of microwave into the forest. In case of the canopy model for mountain forest areas, the factor to account for the vegetation path length is $h_v \cos(\varphi)/\cos(\theta)$, where h_v is the canopy height and $m = \cos(\varphi)/\cos(\theta)$ is the function of the direction vector $[\cos(\theta)$ and $\cos(\varphi)$

Table 5 Power of three scattering components over two study areas.

Method	Mountain forest area A			Forest area B		
	P_s (%)	P_d (%)	P_v (%)	P_s (%)	P_d (%)	P_v (%)
Adaptive	11.86	18.61	69.53	3.85	7.90	88.25
STSM	21.19	16.96	61.85	3.46	6.13	90.41

are presented as in Eqs. (5) and (7), respectively]. Thereby, the occurrences of the ground trunk double-bounce scattering are not as many as those of single-bounce scattering directly from the trunks or branches. Therefore, the reduced volume scattering power mainly changes into the single-bounce scattering.

5 Conclusion

An STSM for forest height estimation over mountain forest areas using L-band single-baseline PolInSAR data is proposed, which consists of three layers: canopy, tree trunk, and ground layer. In the STSM, the phase and parameters of canopy layer are extracted by using the hybrid decomposition technique based on interferometric coherence and polarimetric coherence matrices, and underlying ground topography phase and parameters of ground and tree trunk layer are estimated by a constrained optimization iterative technique. In comparison to other methods, the STSM enables us to improve the accurate estimation of forest height and ground topography over mountain forest area, as well as to retrieve additional parameters related to the degree of randomness, the mean orientation of the particles, the canopy layer depth, effective particle scattering anisotropy, the canopy fill factor, the tree trunk height, and power contribution of each scattering component. The STSM is quite flexible and effective for analysis of more complex multilayer forest model with PolInSAR images. The experimental results indicate that the forest parameters can be retrieved directly and more accurately by the proposed approach. In the future, further theoretical and experimental investigations will be done to improve the performance of the proposed approach.

Appendix

The polarimetric scattering matrix for a particle in the random volume is given by

$$S_v = \begin{bmatrix} s_h & 0 \\ 0 & s_v \end{bmatrix}. \tag{29}$$

The particle scattering anisotropy is determined from the backscattering coefficient independently of orientation and scattered power via

$$\delta = \left(\frac{s_h - s_v}{s_h + s_v} \right)^*. \tag{30}$$

The coherence matrix of a single scatterer with backscattering anisotropy δ and OA θ are expressed as follows:

$$T(\theta, \delta) = R_{T(2\theta)} \begin{bmatrix} 1 & \delta & 0 \\ \delta^* & |\delta|^2 & 0 \\ 0 & 0 & 0 \end{bmatrix} R_{T(2\theta)}^T \quad \text{with} \quad R_{T(2\theta)} = \begin{bmatrix} 1 & 0 & 0 \\ 0 & \cos(2\theta) & \sin(2\theta) \\ 0 & -\sin(2\theta) & \cos(2\theta) \end{bmatrix}. \tag{31}$$

Assuming a volume with a von Mises distribution of orientation with probability density function as follows:

$$p(\theta) = p_c(\theta|\overline{\theta}, \kappa) = \frac{e^{\kappa \cos 2(\theta - \overline{\theta})}}{\pi I_0(\kappa)}, \tag{32}$$

where κ is the degree of concentration and $I_0(\kappa)$ is the modified Bessel function of order 0. Then, the expected values of the coherence matrix entries are given by

$$\langle T_{v(ij)}(\delta, \overline{\theta}) \rangle = \int_0^{2\pi} T_{v(ij)}(\delta, \theta) p_c(\theta|\overline{\theta}, \kappa) \mathrm{d}\theta = \frac{1}{\pi I_0(\kappa)} \int_{-\frac{\pi}{2}}^{\frac{\pi}{2}} T_{v(ij)}(\delta, \theta) e^{\kappa \cos 2(\theta - \overline{\theta})} \mathrm{d}\theta. \tag{33}$$

We note that

$$\cos \theta = \cos \theta' \cos \overline{\theta} - \sin \theta' \sin \overline{\theta}, \quad \sin \theta = \cos \theta' \sin \overline{\theta} + \sin \theta' \cos \overline{\theta}, \tag{34}$$

with

$$\theta' = \theta - \overline{\theta} \in [0; 2\pi].$$

Note that

$$\int_0^\pi e^{\kappa \cos(2\theta)} \sin(2n\theta) \mathrm{d}\theta = 0; \qquad I_n(\kappa) = \frac{1}{\pi} \int_0^\pi e^{\kappa \cos(2\theta)} \cos(2n\theta) \mathrm{d}\theta, \tag{35}$$

where I_n are the modified Bessel function of n'th order.

Then, the elements of coherence matrix are determined as follows:

$$T_{11} = \int_0^\pi p(\theta|\overline{\theta}, \kappa) \mathrm{d}\theta = \frac{1}{\pi I_0(\kappa)} \int_0^\pi e^{\kappa \cos[2(\theta - \overline{\theta})]} \mathrm{d}\theta = 1, \tag{36}$$

$$\begin{aligned}
T_{12} &= \int_0^\pi \delta p(\theta|\overline{\theta}, \kappa) \cos(2\theta) \mathrm{d}\theta \\
&= \frac{\delta}{\pi I_0(\kappa)} \int_{-\pi/2}^{\pi/2} e^{\kappa \cos[2(\theta - \overline{\theta})]} [\cos(2\theta') \cos(2\overline{\theta}) - \sin(2\theta') \sin(2\overline{\theta})] \mathrm{d}\theta' \\
&= \delta \cos(2\overline{\theta}) \frac{1}{\pi I_0(\kappa)} \int_{-\pi/2}^{\pi/2} e^{\kappa \cos(2\theta')} \cos(2\theta') \mathrm{d}\theta' = \delta \cos(2\overline{\theta}) \frac{I_1(\kappa)}{I_0(\kappa)}, \tag{37}
\end{aligned}$$

$$\begin{aligned}
T_{13} &= -\int_0^\pi \delta p(\theta|\overline{\theta}, \kappa) \sin(2\theta) \mathrm{d}\theta \\
&= -\frac{\delta}{\pi I_0(\kappa)} \int_{-\pi/2}^{\pi/2} e^{\kappa \cos[2(\theta - \overline{\theta})]} [\cos(2\theta') \sin(2\overline{\theta}) - \sin(2\theta') \cos(2\overline{\theta})] \mathrm{d}\theta' \\
&= -\delta \sin(2\overline{\theta}) \frac{1}{\pi I_0(\kappa)} \int_{-\pi/2}^{\pi/2} e^{\kappa \cos(2\theta')} \cos(2\theta') \mathrm{d}\theta' = -\delta \sin(2\overline{\theta}) \frac{I_1(\kappa)}{I_0(\kappa)}, \tag{38}
\end{aligned}$$

$$T_{21} = T_{12}^* = \delta^* \cos(2\overline{\theta}) \frac{I_1(\kappa)}{I_0(\kappa)}, \tag{39}$$

$$\begin{aligned}
T_{22} &= \int_{-\pi/2}^{\pi/2} |\delta|^2 p(\theta|\overline{\theta}, \kappa) \cos^2(2\theta) \mathrm{d}\theta = \frac{|\delta|^2}{\pi I_0(\kappa)} \int_{-\pi/2}^{\pi/2} e^{\kappa \cos[2(\theta - \overline{\theta})]} \left[\frac{1 + \cos(4\theta)}{2} \right] \mathrm{d}\theta \\
&= \frac{|\delta|^2}{2\pi I_0(\kappa)} \int_{-\pi/2}^{\pi/2} e^{\kappa \cos(2\theta')} \mathrm{d}\theta' + \frac{|\delta|^2 \cos(4\overline{\theta})}{2\pi I_0(\kappa)} \int_{-\pi/2}^{\pi/2} e^{\kappa \cos(2\theta')} \cos(4\theta') \mathrm{d}\theta' \\
&= \frac{|\delta|^2}{2} \left[1 + \frac{I_2(\kappa)}{I_0(\kappa)} \cos(4\overline{\theta}) \right], \tag{40}
\end{aligned}$$

$$T_{23} = -\int_{-\pi/2}^{\pi/2} |\delta|^2 p(\theta|\overline{\theta}, \kappa) \cos(2\theta) \sin(2\theta) d\theta = -\frac{|\delta|^2}{\pi I_0(\kappa)} \int_{-\pi/2}^{\pi/2} e^{\kappa \cos[2(\theta-\overline{\theta})]} \left[\frac{\sin(4\theta)}{2}\right] d\theta$$

$$= -\frac{|\delta|^2 \sin(4\overline{\theta})}{2\pi I_0(\kappa)} \int_{-\pi/2}^{\pi/2} e^{\kappa \cos(2\theta')} \cos(4\theta') d\theta' = -\frac{|\delta|^2}{2} \frac{I_2(\kappa)}{I_0(\kappa)} \sin(4\overline{\theta}), \tag{41}$$

$$T_{32} = T_{23}^* = -\frac{|\delta|^2}{2} \frac{I_2(\kappa)}{I_0(\kappa)} \sin(4\overline{\theta}), \tag{42}$$

$$T_{33} = \int_{-\pi/2}^{\pi/2} |\delta|^2 p(\theta|\overline{\theta}, \kappa) \sin^2(2\theta) d\theta = \frac{|\delta|^2}{\pi I_0(\kappa)} \int_{-\pi/2}^{\pi/2} e^{\kappa \cos[2(\theta-\overline{\theta})]} \left[\frac{1 - \cos(4\theta)}{2}\right] d\theta$$

$$= \frac{|\delta|^2}{2\pi I_0(\kappa)} \int_{-\pi/2}^{\pi/2} e^{\kappa \cos(2\theta')} d\theta' - \frac{|\delta|^2 \cos(4\overline{\theta})}{2\pi I_0(\kappa)} \int_{-\pi/2}^{\pi/2} e^{\kappa \cos(2\theta')} \cos(4\theta') d\theta'$$

$$= \frac{|\delta|^2}{2} \left[1 - \frac{I_2(\kappa)}{I_0(\kappa)} \cos(4\overline{\theta})\right]. \tag{43}$$

Then, we can obtain the coherence matrix for volume scattering contribution

$$T_v(\delta, \overline{\theta}, \kappa) = \frac{1}{2} \begin{bmatrix} 1 & \delta \cos(2\overline{\theta})g(\kappa) & -\delta \sin(2\overline{\theta})g(\kappa) \\ \delta^* \cos(2\overline{\theta})g(\kappa) & \frac{|\delta|^2}{2}[1 + \cos(4\overline{\theta})g_c(\kappa)] & -\frac{|\delta|^2}{2} \sin(4\overline{\theta})g_c(\kappa) \\ -\delta^* \sin(2\overline{\theta})g(\kappa) & -\frac{|\delta|^2}{2} \sin(4\overline{\theta})g_c(\kappa) & \frac{|\delta|^2}{2}[1 - \cos(4\overline{\theta})g_c(\kappa)] \end{bmatrix}$$

$$= [T_a(\delta)] + g(\kappa)[T_b(\delta, 2\overline{\theta})] + g_c(\kappa)[T_c(\delta, 2\overline{\theta})]. \tag{44}$$

With

$$g(\kappa) = \frac{I_1(\kappa)}{I_0(\kappa)} \quad \text{and} \quad g_c(\kappa) = \frac{I_2(\kappa)}{I_0(\kappa)}, \tag{45}$$

$$[T_a(\delta)] = \frac{1}{4} \begin{bmatrix} 2 & 0 & 0 \\ 0 & |\delta|^2 & 0 \\ 0 & 0 & |\delta|^2 \end{bmatrix}; \quad [T_b(\delta, 2\overline{\theta})] = \frac{1}{4} \begin{bmatrix} 0 & 2\delta \cos 2\overline{\theta} & -2\delta \sin 2\overline{\theta} \\ 2\delta^* \cos 2\overline{\theta} & 0 & 0 \\ -2\delta^* \sin 2\overline{\theta} & 0 & 0 \end{bmatrix},$$

$$[T_c(\delta, 4\overline{\theta})] = \frac{1}{4} \begin{bmatrix} 0 & 0 & 0 \\ 0 & |\delta|^2 \cos 4\overline{\theta} & -|\delta|^2 \sin 4\overline{\theta} \\ 0 & -|\delta|^2 \sin 4\overline{\theta} & -|\delta|^2 \cos 4\overline{\theta} \end{bmatrix}. \tag{46}$$

The degree of orientation randomness τ is defined independently of the OA pdf as the area under $p(\theta - \overline{\theta})$ divided by the area of the smallest enclosing box in the range $\theta \in [-\pi/2, \pi/2]$. Then, the degree of orientation randomness can be obtained as

$$\tau = \frac{\int p_c(\theta - \overline{\theta}) d\theta}{\pi \max\{p_c(\theta)\}} = I_0(\kappa) e^{-\kappa}. \tag{47}$$

The parameter κ ranges from zero to infinity. In practice, there is little difference between distributions with values of κ larger than about 34 or so. It can be shown that the degree of orientation randomness τ can be evaluated in terms of κ. We can calculate the values of $g(\kappa)$, $g_c(\kappa)$, and τ by varying κ, and then we can fit polynomials to these calculated points. The following are fifth- order polynomials $p(\tau)$ and $q(\tau)$ [see Eq. (48)], which provide accuracy around $1e - 10$ on given κ

$$p(\tau) = -75.6267\tau^5 + 179.9431\tau^4 - 149.8697\tau^3 + 53.1108\tau^2 - 9.0582\tau + 1.5008,$$

$$q(\tau) = -30.0764\tau^5 + 72.6174\tau^4 - 64.3342\tau^3 + 28.4209\tau^2 - 8.1212\tau + 1.4936. \tag{48}$$

Acknowledgments

References

1. FAO, *Global Forest Resources Assessment 2005*, FAO Forestry Paper 147 (2005).
2. S. R. Cloude and K. P. Papathanassiou, "Three-stage inversion process for polarimetric SAR interferometric," *IEE Proc. Radar Sonar Navig.* **150**(3), 125–134 (1998).
3. H. Yamada et al., "Polarimetric SAR interferometry for forest analysis based on the ESPRIT algorithm," *IEICE Trans. Electron.* **84**(12), 1917–2014 (2001).
4. H. Yamada, M. Yamazaki, and Y. Yamaguchi, "On scattering model decomposition of PolSAR and its application to ESPRIT-base Pol-InSAR," in *Proc. of 6th European Conf. on Synthetic Aperture Radar*, Dresden, Germany (2006).
5. H. Yamada, M. Yamazaki, and Y. Yamaguchi, "On scattering model decomposition of PolSAR and its application to ESPRIT-based PolInSAR," in *Proc. of 6th European Conf. on Synthetic Aperture Radar* (2006).
6. F. Garestier and T. Le Toan, "Evaluation of forest modeling for forest height estimation using P-band PolInSAR data," in *Proc. BIOGEOSAR*, Bari, Italy (2007).
7. F. Garestier and T. Le Toan, "Forest modeling for forest height inversion using single baseline InSAR/PolInSAR data," *IEEE Trans. Geosci. Remote Sens.* **48**(3), 1528–1539 (2010).
8. F. Garestier and T. Le Toan, "Estimation of the backscatter vertical profile of a pine forest using single baseline P-band (Pol-) InSAR data," *IEEE Trans. Geosci. Remote Sens.* **48**(9), 3340–3348 (2010).
9. J. D. Ballester-Bermand and J. M. Lopez-Sanchez, "Applying the Freeman–Durden decomposition concept to polarimatric SAR interferometry," *IEEE Trans. Geosci. Remote Sens.* **48**(1), 466–479 (2010).
10. M. Neumann, L. F. Famil, and A. Reigber, "Estimation of forest structure, ground and canopy layer characteristics from multibaseline polarimetric interferometric SAR data," *IEEE Trans. Geosci. Remote Sens.* **48**(3), 1086–1104 (2010).
11. S. R. Cloude and K. P. Papathanassiou, "Polarimetric SAR interferometry," *IEEE Trans. Geosci. Remote Sens.* **36**(5), 1551–1565 (1998).
12. J. S. Lee and T. L. Anisworth, "The effect of orientation angle compensation on coherence matrix and polarimetric target decomposition," *IEEE Trans. Geosci. Remote Sens.* **49**(1), 53–64 (2011).
13. J. J. VanZyl, "The effect of topography on the radar scattering from vegetated areas," *IEEE Trans. Geosci. Remote Sens.* **31**(1), 153–160 (1993).
14. S. R. Cloude, *Polarization Application in Remote Sensing*, pp. 265–270, Oxford University Press, New York (2009).
15. H. Cai, B. Zou, and M. Lin, "Parameter inversion models based on PolInSAR images," in *Proc. of IEEE Asia-Pacific Conf. on Synthetic aperture radar (APSAR)*, Huangshan, China, Vol. **1**, pp. 751–754 (2007).
16. B. Zou et al., "Building parameters extraction from spaceborne PolInSAR image using a built-up area scattering model," *IEEE J. Sel. Top. Appl. Earth Obs. Remote Sens.* **6**(3), 162–170 (2013).
17. R. N. Treuhaft and P. Siqueria, "Vertical structure of vegetated land surface from interferometric and polarimetric radar," *Radio Sci.* **35**(1), 141–177 (2000).
18. A. Freeman and S. L. Durden, "A three component scattering model to describe polarimetric SAR data," *IEEE Trans. Geosci. Remote Sens.* **36**(3), 963–973 (1998).
19. S. R. Cloude and E. Pottier, "A review of target decomposition theorems in radar polarimetry," *IEEE Trans. Geosci. Remote Sens.* **34**(2), 498–518 (1996).
20. S. Park, W. Moon, and E. Pottier, "Assessment of scattering mechanism of polarimetric SAR signal from mountain forest areas," *IEEE Trans. Geosci. Remote Sens.* **50**(11), 4711–4719 (2012).

21. I. Hajnsek, E. Pottier, and S. R. Cloude, "Inversion of surface parameters from polarimetric SAR," *IEEE Trans. Geosci. Remote Sens.* **41**(7), 727–744 (2003).
22. J. Xu et al., "Using similarity parameters for supervised polarimetric SAR image classification," *IEICE Trans. Commun.* **85**(12), 2934–2942 (2002).
23. L. Zhang, B. Zou, and W. Tang, "Polarimetric interferometric eigenvalue similarity parameter and its application in target detection," *IEEE Geosci. Remote Sens. Lett.* **8**(4), 819–823 (2011).
24. Z. Jiao et al., "The modified three-component decomposition method for polarimetric SAR data," *IEEE Geosci. Remote Sens. Lett.* **11**(1), 200–204 (2014).
25. M. L. Williams, "PolSARproSim: a coherent, polarimetric SAR simulation of forest for PolSARPro," http//earth.eo.esa.int/polsarpro/SimulatedDataSources.html (December 2006).
26. K. P. Papathanassiou and S. R. Cloude, "The effect of temporal decorrelation on the inversion of forest parameters from PolInSAR data," in *Proc. of IEEE Int. Conf. on Geoscience and Remote Sensing Symp.*, Toulouse, France, 21–25 July 2003, pp. 1429–1431 (2003).
27. N. P. Minh and B. Zou, "A novel algorithm for forest height estimation using PolInSAR image," *Int. J. Signal Process. Image Process. Pattern Recognit.* **6**(2), 15–32 (2013).

Nghia Pham Minh received his BS and MS degrees in electronic engineering from Le Qui Don Technical University, Vietnam, in 2005 and 2008, respectively, and his PhD in information and communication engineering from Harbin Institute of Technology, China, in 2014. He is currently a lecturer at Le Qui Don Technical University and visiting lecturer at Duy Tan University, Vietnam. He is currently focusing on polarimetric synthetic aperture radar image processing, polarimetric SAR interferometry, and signal processing.